Polarization-Sensitive Photodetector Based on $GaAs_{1-x}N_x$

V.G. Ibarra-Sierra,[1] J.C. Sandoval-Santana,[1] R.S. Joshya,[2] H. Carrère,[2] L.A. Bakaleinikov,[3] V. K. Kalevich,[3] E.L. Ivchenko,[3] X. Marie,[2] T. Amand,[2] A. Balocchi,[2] and A. Kunold[1,*]

[1] *Área de Física Teórica y Materia Condensada, Universidad Autónoma Metropolitana Azcapotzalco, Av. San Pablo 180, Col. Reynosa-Tamaulipas, Cuidad de México 02200, Mexico*

[2] *Universitè de Toulouse, INSA-CNRS-UPS, LPCNO, 135 Avenue de Rangueil, Toulouse 31077, France*

[3] *Ioffe Physical-Technical Institute, St. Petersburg 194021, Russia*

(Received 20 February 2021; revised 19 April 2021; accepted 26 May 2021; published 16 June 2021)

We propose and numerically simulate an optoelectronic compact circular polarimeter. It allows for electrical measurement of the degree of circular polarization and light intensity at room temperature for a wide range of incidence angles in a single shot. The device, being based on $GaAs_{1-x}N_x$, is easy to integrate into standard electronics and does not require bulky movable parts nor extra detectors. Its operation hinges mainly on two phenomena: the spin-dependent capture of electrons and the hyperfine interaction between bound electrons and nuclei on Ga^{2+} paramagnetic centers in $GaAs_{1-x}N_x$. The first phenomenon confers the device with sensitivity to the degree of circular polarization and the latter phenomenon allows one to discriminate the handedness of the incident light.

DOI: 10.1103/PhysRevApplied.15.064040

I. INTRODUCTION

Just as frequency and intensity, polarization is one of the fundamental properties of light. In particular circular polarimetry, the determination of the degree of circular polarization, plays a determinant role in many recent technological developments. The capacity of circularly polarized light to interact with chiral biological structures has given rise to a wide range of applications that go from remote sensing of microbial organisms [1] to medical assessment techniques [2–4]. The detection of circularly polarized photon states is key to quantum information processing in the observation of entanglement between photons and electronic [5,6] or nuclear [7,8] spins.

The detection of circularly polarized light conventionally requires light to pass through a sequence of various hefty optical elements [9] such as rotating polarizers and waveplates hampering the integration of circular polarimeters to standard electronics [10].

To circumvent the issues posed by standard circular polarimetry, many circular polarizer architectures have been proposed. Although organic photovoltaics [11] has allowed flexible and tunable full-Stokes polarimeters [12,13] to be built from naturally abundant materials, it requires the stacking of multiple components. The distinct optical response of plasmonic chiral metamaterials to left-handed (LHCP) and right-handed (RHCP) light has been exploited to realize circular polarizers [10,14–17]. Despite the relative ease with which these structures can be merged with standard electronics [14], they are limited by low circular polarization extinction ratios and low optical efficiency [10] due to the losses of the parasitic currents generated in the nanoinclusions [18]. Regarding the compactness of the device, a major drawback of these structures is the requirement of an off-chip detector to sense the scattered light [18]. Similar approaches have been taken in the use of chiral inclusions in dielectric metasurfaces [16] and transition metal dichalcogenides [19]. Even though the more recent Fabry-Pérot cavity-based polarimeters [20] can, in principle, be extended to circularly polarized light measurements, so far they have only been demonstrated to have low signal-to-noise ratios under linearly polarized light. The silicon-on-insulator [18,21,22] is probably the most robust platform for the integration of polarimeters with microelectronics because of their compatibility with the metal oxide semiconductor fabrication process [22].

Spin-optoelectronic devices employ the coupling of photon angular momentum and electron spin [23–25]. These devices rely on the photogeneration of spin-polarized conduction-band electrons due to the unique optical selection rules of zinc-blende semiconductors under circularly polarized light. Through the spin-orbit interaction the light-polarization information can be translated first into an electron spin polarization and then into an electrical signal via the inverse spin-Hall effect [23]. Other similar alternatives convert the electron spin polarization into a photovoltage through the asymmetries in the electron motion due the built-in electric field induced by the Shottky contacts of the device [24]. Inverse spin-Hall effect devices operate at room temperature [23,26] but allow one

*akb@azc.uam.mx

 © 2021 American Physical Society

only to detect the degree of circular polarization of light. In contrast, Shottky devices can detect simultaneously the degree of circular polarization and intensity in a single shot but are restricted to cryogenic temperatures.

In this paper we propose a spin-optoelectronic device for the simultaneous detection of the intensity and degree of circular polarization at room temperature. The detector is based on a $GaAs_{1-x}N_x$ epilayer grown on GaAs. The detection scheme relies mainly on two phenomena: the generation of spin-polarized conduction-band (CB) electrons through optically oriented pumping and the spin-dependent recombination (SDR) [27–55] that the CB electrons undergo through Ga^{2+} paramagnetic centers [35,39,44,54]. The orientation of the circularly polarized light (RHCP or LHCP) is discriminated from the sign of the so-called Overhauser-like effective magnetic field [29,45,49,50].

The paper is organized as follows. In Sec. II we outline how the incidence power and the degree of circular polarization affect the conductivity as a function of an applied magnetic field. The device architecture and the procedure to deconvolve these quantities from the conductivity are sketched in Sec. III. In Sec. IV we show a comparison between the proposed device and other circular polarimeters. In the Appendix we present a detailed description of the model based on a master equation for the density matrix that permits the computation of the most relevant parameters to obtain the conductivity of the sample. We also include a description in the Appendix of the method followed to fit the model parameters through measurements of the photoluminescence.

II. DETECTION OF THE DEGREE OF CIRCULAR POLARIZATION THROUGH THE SPIN FILTERING EFFECT

SDR produces an unbalance between the two CB electron spin polarization populations under circularly polarized light excitation. The unbalance is provoked by the different capture times that hinge on the relative spin orientation of CB electrons and the Ga^{2+} center's bound electron [34,35,41]. Whereas parallel-oriented spins block CB electrons from recombining, antiparallel ones promote recombination to the centers. This sets in motion a spin filtering effect in which electrons with a given spin orientation remain in the CB for long times, while those with the opposite spin polarization quickly recombine to the centers. Spin polarizations close to 100% can be attained after a few of these recombination cycles [49] at room temperature and over a wide wavelength excitation range [56]. The generated spin-polarized CB electron excess population largely enhances the photoconductivity under circularly polarized illumination as compared to linearly polarized illumination [38,42]. A similar argument applies to the holes left behind by the photoexcited electrons. The spin-dependent photoconductivity thus provides the means to transduce the degree of electron spin polarization into an electrical signal.

Even though it can be modulated by the degree of spin polarization, the conductivity itself does not allow one to discriminate between RHCP and LHCP light; it is not sensitive to the spin direction of the excess CB electrons and nor, consequently, to the circular polarization handedness of the incident light. However, RHCP and LHCP light can be made to have different effects on the Ga^{2+} centers by applying a relatively small magnetic field in the Faraday configuration. This primarily has two effects: first, it amplifies the spin filtering effect [43,45–47] and second, it generates an Overhauser-like magnetic field. The main cause of these two phenomena has been identified as the hyperfine interaction between the outer shell bound electron and the nucleus of the Ga^{2+} center [46–49,51]. The amplification of the spin filtering effect gives the photoluminescence intensity as a function of the magnetic field the shape of an inverted Lorentzian function whose minimum is located at the Overhauser-like magnetic field [29,45,49,50]. The position of this minimum or, more precisely, the sign of the Overhauser-like magnetic field is key to differentiating between the two orientations of circularly polarized light. The Overhauser-like magnetic field is positive for RHCP and negative for LHCP light.

Figure 1 shows plots of the calculated longitudinal conductivity σ_{xx} as a function of the magnetic field for linearly polarized light (X, green), right-circularly polarized light (σ^+, solid blue line), and left-circularly polarized light (σ^-, dashed blue line). The electrical current is calculated through the Drude model. The setup is sketched in Fig. 1(a). We consider rectangular $GaAs_{1-x}N_x$ slabs of length L, width w, and height h subject to a perpendicular magnetic field B and a bias voltage V_b applied along the length L [see Fig. 1(a)]. The longitudinal component of the conductivity is given by the sum of the electron, light hole, and heavy hole contributions:

$$\sigma_{xx} = e\left[\frac{\bar{n}\mu_e}{1+\mu_e^2B^2} + \frac{\bar{p}\mu_{lh}/2}{1+\mu_{lh}^2B^2} + \frac{\bar{p}\mu_{hh}/2}{1+\mu_{hh}^2B^2} + \frac{[\bar{n}\mu_e^2B/(1+\mu_e^2B^2) - (\bar{p}\mu_{lh}^2B/2)/(1+\mu_{lh}^2B^2) - (\bar{p}\mu_{hh}^2B/2)/(1+\mu_{hh}^2B^2)]^2}{\mu_e\bar{n}/(1+\mu_e^2B^2) + (\mu_{lh}\bar{p}/2)/(1+\mu_{lh}^2B^2) + (\mu_{hh}\bar{p}/2)/(1+\mu_{hh}^2B^2)}\right]. \quad (1)$$

Here e is the electron charge, $\mu_e = 300$ cm^2/Vs, $\mu_{lh} = 50$ cm^2/Vs, and $\mu_{hh} = 50$ cm^2/Vs [57–62] are the electron, light hole, and heavy hole mobilities. For such a configuration, the current intensity is given by

$$I = \sigma_{xx}(V_b/L)wh. \tag{2}$$

The electron and hole densities $\bar{n}$ and $\bar{p}$, needed in the expressions above, are obtained from the quantum statistical averages of the density matrix; see Eqs. (A31) and (A32). The density matrix is obtained from the numerical solution of a master equation based on a model previously developed by us [63]. The main difference between the previous and current master equation approaches is the inclusion of a dissipator that allows us to set different relaxation times for electronic spins, nuclear spins, and electron-nucleus spin correlations in the Ga^{2+} traps. This dissipator allows us to obtain a better quantitative agreement between the experimental and theoretical results. Among other things, this is key to accurately predicting the Overhauser-like effective magnetic field, which is a crucial parameter for the device operation, as we discuss below. In the Appendix we present a detailed description of the master equation approach and list the input parameters.

The second line of Eq. (1) comes from the transverse Hall field. These terms also introduce a magnetic field dependence in σ_{xx}, but they are far exceeded by that introduced by $\bar{n}$ and $\bar{p}$. Indeed, the inverted Lorentzian shape of this curve comes entirely from $\bar{n}$ and $\bar{p}$ as functions of the magnetic field. These curves strongly resemble the inverted Lorentzian obtained for the photoluminescence [43], a trait of the amplification of the spin filtering effect under a Faraday configuration magnetic field. This particular behavior enters the conductivity in Eq. (1) through the electron and hole densities. We observe that the conductivity is enhanced when the illumination is switched to σ^+ or σ^-. This difference (green shaded region) permits us to distinguish between linearly and circularly polarized incident light. One of the most significant characteristics of these plots is the different displacements created by σ^+ and σ^- incident light. While the incident RHCP light shifts the Lorentzian curve 12 mT to the right, the LHCP light shifts it to the left by the same amount. The contrast between these two curves (blue shaded region) allows us to discriminate between RHCP and LHCP light. Comparing panel (b) with panels (c) and (d) we note that either increasing the illumination power P_{exc} (from 20 to 30 mW) or its degree of circular polarization P_c (from 20% to 40%) appreciably changes some of the $\sigma_{xx}(B)$ features. Particular attention should be paid to the Overhauser-like magnetic field B_N and the Lorentzian width ΔB. These two quantities are known to be constant functions of the power intensity after they saturate [45,63] at a threshold power that, in this case, is roughly 10 mW. Below, this property of B_N and ΔB will be important for selecting the relevant parameters used to characterize some of the properties of light as incident power, degree of circular polarization, and relative angle.

The incidence angle of circularly polarized light also has a strong impact on the conductivity of the sample. A complete analysis of its multiple effects outside normal incidence requires considering the variations of the intensity, propagation direction, and the polarization predicted by the Fresnel equations and the Snell law. These depend on the widths of the GaAs cap, present in some architectures, and the $GaAs_{1-x}N_x$ slab. This would, however, yield sample-geometry-dependent conductivities. So as to obtain data of a more general nature, it is convenient to express our results in terms of the relative angle θ between the applied magnetic field and the propagation line of light inside the sample. Given its isotropy, the model (presented in the Appendix) is sensitive only to the relative orientation of the applied magnetic field and the propagation direction of light inside the sample. This reduces the number of used variables and considerably simplifies the discussion. Even though the angle θ has a noticeable effect on the conductivity, it is still possible to carry out undistorted intensity and degree of circular polarization measurements. In Fig. 2 we observe the conductivity as a function of the magnetic field for angles between 0° (Faraday configuration) to 90° (Voigt configuration). A sketch of the setup is presented in Fig. 2(a) We observe that at Faraday geometry ($\theta = 0°$) the $\sigma_{xx}(B)$ adopts the features of the amplification of the spin filtering effect, namely, it takes the form of a downward Lorentzian-like curve shifted by B_N. Meanwhile, at Voigt geometry ($\theta = 90°$), $\sigma_{xx}(B)$ takes the shape of the upward centered Lorentzian that characterizes the Hanle effect [36]. At oblique angles the conductivity behaves as a combination of both downward and upward Lorentzians [50]. In panel (b) we use as reference $\sigma_{xx}(B)$ under illumination with an incident power of 20 mW and a degree of circular polarization of 20%. The conductivity in panel (b) is contrasted with the conductivity calculated for an incident power of 30 mW in panel (c) and 40% degree of circular polarization in panel (d). We note that, even for very wide relative angles ($\theta \leq 70°$), there is a clear distinction between σ^+ and σ^-. The most efficient detection configuration is at normal incidence where this difference is maximized. We show below that even at wide relative angles it is possible to measure the intensity and the degree of circular polarization.

From Fig. 1, it can then be said that the intensity, the degree of circular polarization, and its handedness are encoded in $\sigma_{xx}(B)$. It still remains to find a way to deconvolve P_{exc}, P_c, and θ from the conductivity. For this purpose, we define the two parameters

$$\Delta_1(B) = \sigma_{xx}(-B) + \sigma_{xx}(B), \tag{3}$$

$$\Delta_2(B) = \sigma_{xx}(-B) - \sigma_{xx}(B), \tag{4}$$

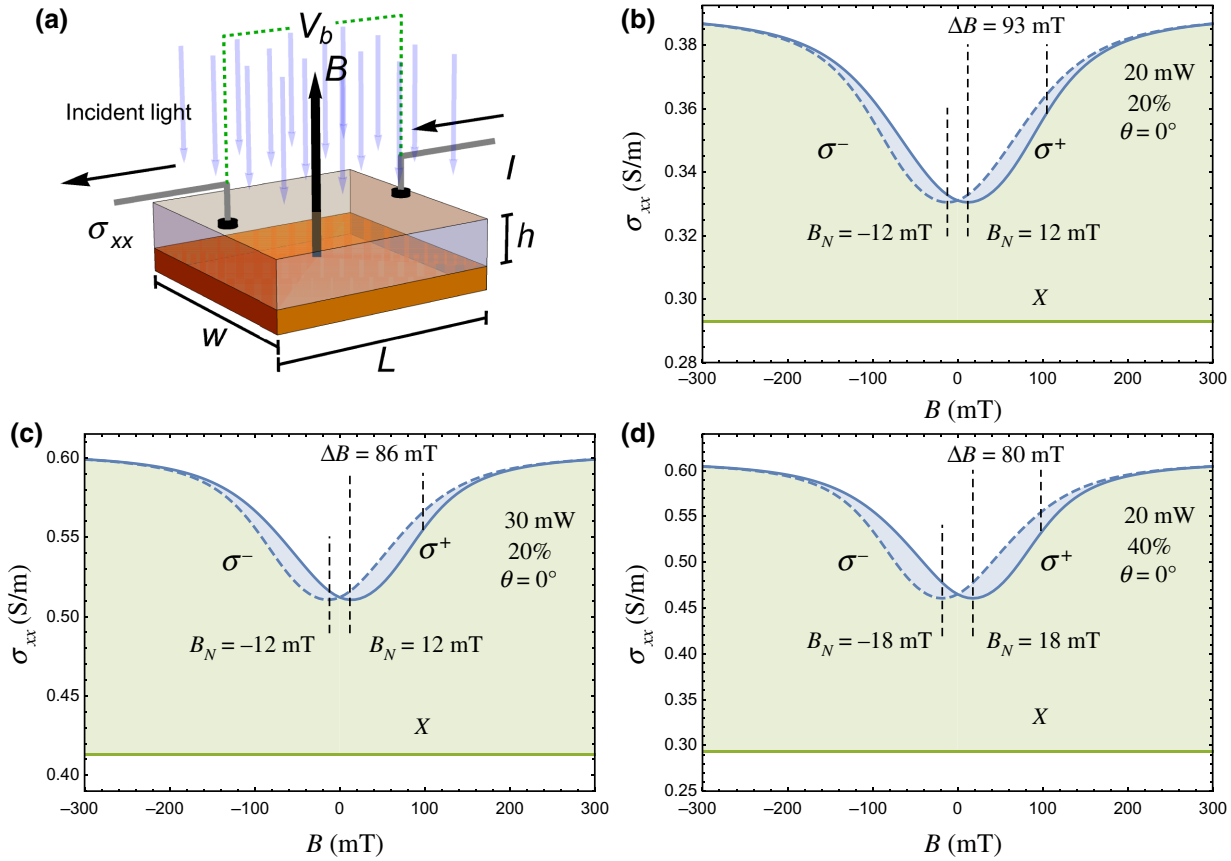

FIG. 1. Longitudinal conductivity σ_{xx} as a function of the magnetic field in the Faraday configuration ($\theta = 0°$) for linearly (X), right-circularly (σ^+) and left-circularly (σ^-) polarized light. (a) Setup sketch of the $GaAs_{1-x}N_x$ slab, magnetic field, and incident light excitation. The magnetic field B is in the Faraday configuration and the conductivity σ_{xx} is determined from the current i and the bias voltage V_b. The incident light power and the degree of circular polarization are set to (b) 20 mW and 20%, (c) 30 mW and 20%, and (d) 20 mW and 40%.

which are plotted in Fig. 3 as a function of the magnetic field. The parameter $\Delta_1(B)$ depends both on the incident power [panel (a)] and degree of circular polarization [panel (b)]. It is however insensitive to the orientation of the circular polarization. Additionally, it is a fairly smooth function of the magnetic field and can therefore be expected to provide information on the power and the degree of circular polarization regardless of the applied magnetic field. Instead, $\Delta_2(B)$ has a pronounced sensitivity to power [panel (c)] and both the degree of circular polarization [panel (c)] and its orientation [panels (c) and (d)] at approximately $B = 50$ mT. This value depends on B_N and ΔB that, as mentioned earlier, remain constant above a certain power threshold. Because of this, the maximum sensitivity of $\Delta_2(B)$ to the power and degree of circular polarization always occurs at the same magnetic field value. The fact that both parameters are very sensitive at fixed values of the magnetic field is central to the design of the polarimeter architecture; not only is no variable magnetic field needed to characterize light, but its magnitude is small enough that it can be generated by small permanent magnets.

The previous results give us an inkling on what parameters may encode all the information necessary to characterize light's degree of circular polarization and power. We know that at $B = 50$ mT, $\Delta_1(B)$ and $\Delta_2(B)$ are strongly responsive to changes in the power and degree of circular polarization. Moreover, the sign of $\Delta_2(50\ \text{mT})$, being a measure of the asymmetry, provides information on the handedness of the degree of polarization. Thereby, a suitable set of parameters to fully characterize an incident beam of light is

$$\Gamma_1 = \Delta_1(50\ \text{mT}), \qquad \Gamma_2 = \Delta_2(50\ \text{mT}). \tag{5}$$

In the next section we propose a device architecture that allows us to measure these two parameters and explain how to extract from them the incidence power P_{exc}, the degree of circular polarization P_c, and its handedness.

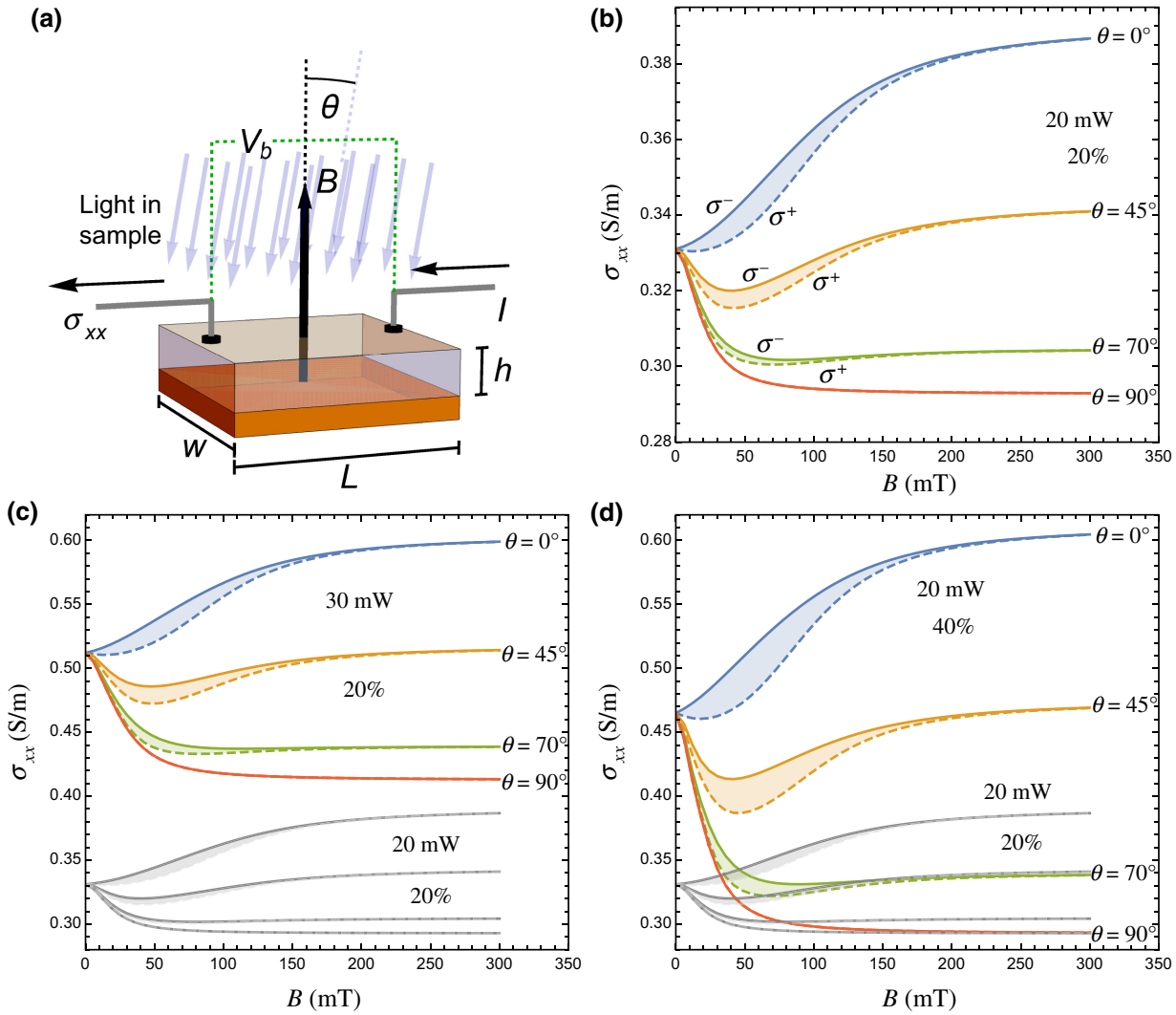

FIG. 2. Longitudinal conductivity σ_{xx} as a function of the magnetic field for different relative angles, power intensities, and degrees and orientations of circularly polarized light. (a) Setup sketch of the $GaAs_{1-x}N_x$ slab, the applied magnetic field, and an incident light excitation. The relative angle θ between the magnetic field and the propagation direction of light inside the sample is marked above the magnetic field. The conductivity σ_{xx} is determined from the current I and the bias voltage V_b. Different incident light power and degree of circular polarization conditions are presented in the three panels: (b) 20 mW and 40% right circular polarization, (c) 30 mW and 20% right circular polarization, and (d) 20 mW and 40% right circular polarization. Panels (c) and (d) also show the plots for a power of 20 mW and a degree of right circular polarization of 40% for comparison (light gray). The solid and dashed lines correspond to σ^- (LHCP) and σ^+ (RHCP), respectively.

III. DEVICE ARCHITECTURE AND DECONVOLUTION OF THE INCIDENT POWER, DEGREE OF POLARIZATION, AND ITS ORIENTATION

The proposed device consists of interconnected slabs of $GaAs_{1-x}N_x$ as shown in Fig. 4. Each slab is made of a $GaAs_{1-x}N_x$ epilayer on a (100)-oriented semi-insulating GaAs substrate [31,33]. This whole heterostructure is depicted as a transparent parallelepiped. The magnetic fields B_1 and B_2 are produced by permanent magnets beneath the $GaAs_{1-x}N_x$/GaAs heterostructures. The voltage source V_b is used to drive the currents I_1 and I_2 through the $GaAs_{1-x}N_x$ slabs. The voltages V_1 and V_2 in the resistances r allow us to detect the currents I_1 and I_2. The permanent magnet sizes should be chosen so as to generate the magnetic fields $B_1 = -B_2 = 50$ mT, providing enough information to obtain Γ_1 and Γ_2. According to Eqs. (3) and (4), it would seem that three values of the conductivity $[\sigma_{xx}(0)$, $\sigma_{xx}(50$ mT), and $\sigma_{xx}(-50$ mT)] are needed to obtain Γ_1 and Γ_2. This would imply the need for a third extra slab of $GaAs_{1-x}N_x$. However, $\sigma_{xx}(0)$ can be estimated as $[\sigma_{xx}(50\text{ mT}) + \sigma_{xx}(-50\text{ mT})]/2$, restricting the number of slabs to two. An equivalent setup would consist of a

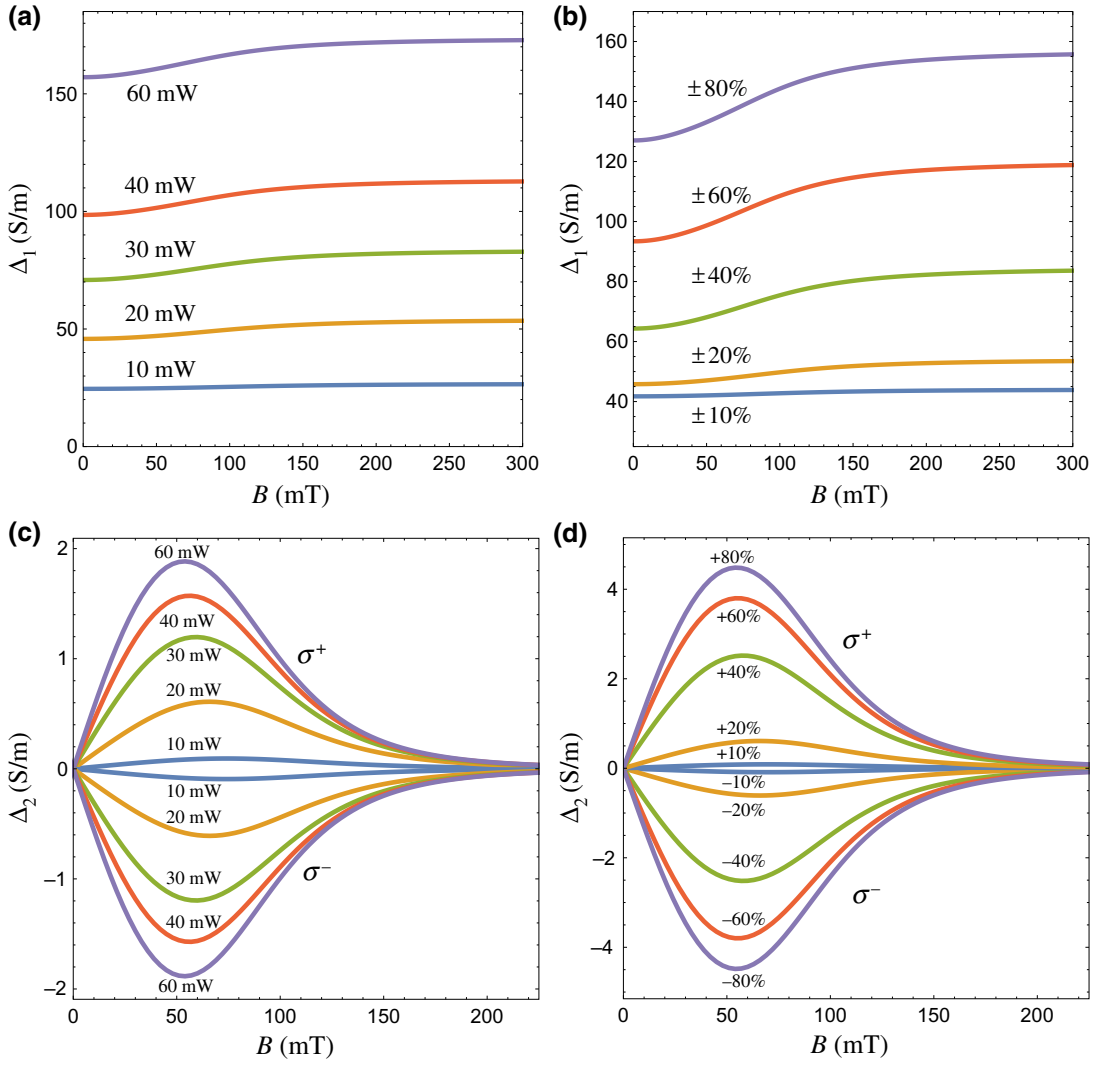

FIG. 3. Parameters (a),(b) $\Delta_1(B)$ and (c),(d) $\Delta_2(B)$ as a function of the magnetic field for different incident powers (a),(c) and degrees of circular polarization (b),(d) for $P_{\text{exc}} = 20$ mW.

single slab of $GaAs_{1-x}N_x$ where a microcoil would generate an alternating magnetic field.

Figures 5 and 6 show the power and degree of polarization isolines on the Γ_1-Γ_2 plane under σ^- and σ^+ illumination. Under normal incidence ($\theta = 0$), the degree of circular polarization P_c and the power P_{exc} can be determined by interpolating between the isolines in Fig. 5(a) or 6(a) depending on whether $\Gamma_2 < 0$ (σ^-) or $\Gamma_2 > 0$ (σ^+). The progression of Figs. 5(a)–5(c) and 6(a)–6(c) shows that, despite the slight deformation due to the variation in the incidence angle, the isolines preserve their main topological properties. Moreover, it can be readily proven from the Fresnel equations that the refracted light remains elliptically polarized even for incidence angles far from $\theta = 0°$. Hence, the values of P_c and P_{exc} can be determined for a very wide range of incidence angles that approximately goes from $\theta = 0°$ to $\theta = 50°$ [10,14–17].

IV. COMPARISON WITH OTHER CIRCULAR POLARIMETERS

To make a comparative analysis with other circular polarimeters, we focus the discussion on four qualitative aspects and three quantitative parameters of the device operation. The qualitative aspects are whether (i) the device can provide the power and degree of circular polarization in a single shot, (ii) it requires an off-chip detector, (iii) it works at room temperature, and whether (iv) it can be integrated to standard electronics. The quantitative aspects are (i) quantum efficiency, (ii) the dissymmetry factor, and (iii) the saturation power. The capacity of the device to discriminate between RHCP and LHCP light is quantified by the dissymmetry factor [70]

$$g_d = \frac{I^R - I^L}{0.5(I^R + I^L)}, \tag{6}$$

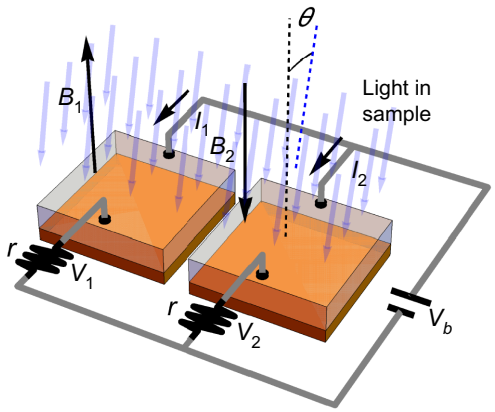

FIG. 4. Schematics of the polarimeter. Both slabs are connected in parallel with a bias voltage source V_b. The voltages in the resistances r, V_1 and V_2, are used to determine the current intensities I_1 and I_2 that travel through each $GaAs_{1-x}N_x$ epilayer slab. The magnetic fields B_1 and B_2 are produced by the permanent magnets (orange) located on the base of each slab. The relative angle θ between the magnetic field and the propagation direction of light inside the sample is indicated.

where I^R and I^L are the currents upon RHCP and LHCP excitation, respectively. In our case,

$$I^R = \sigma_{xx}^R (V_b/L)wh, \qquad I^L = \sigma_{yy}^L (V_b/L)wh, \qquad (7)$$

are the electrical currents [Eq. (2)] at $B = -50$ mT and $B = 50$ mT, where σ_{xx}^R and σ_{xx}^L are the conductivities under RHCP and LHCP illumination, respectively.

In Table I we list the main characteristics of our proposed device and other existing circular polarimeters. In the table we compare our device with chiral metamaterials [10,15–17,66,67], chiral plasmonic flat devices [14], chiral plasmonic $MoSe_2$ metasurfaces [19], photovoltaic spin-Hall detectors [23,24,26], silicon-on-insulator [18,21,22], Fe/MgO/Ge heterostructures [68], organic field-effect transistors [69,70], and perovskite-based photodiodes [71,72].

Plasmonic chiral metamaterials [10,15–17,67] have very good discrimination capabilities but suffer from low circular polarization extinction ratios, low optical efficiency, and require an off-chip detector. They are manufactured through lithographic processes and have multiple layers [67]. Metamaterials work on the principle of hot electron injection and therefore exhibit very low quantum efficiency and, for the moment, work well only on silicon [66], thus having a very limited wavelength range. Plasmonic flat devices [14] can work as full-Stokes polarimeters and have remarkably large dissymetry factors. However, their manufacture involves a patterning process on the substrate with electron beam lithography, and requires an extra detector. Chiral plasmonic $MoSe_2$ metasurfaces [19] exhibit very high dissymetry factors and work for a wide range of wavelengths (640–840 nm). Silicon-on-insulator polarimeters [21,22] are CMOS compatible and provide the four Stokes parameters; they have, however, the disadvantage of having extremely complicated architectures. The spin-optoelectronic detectors [23,26] combine the spin-Hall and the photovoltaic effects through a Au/InP hybrid structure to measure the degree of circular polarization and power simultaneously [24]. Fe/MgO/Ge(001) heterostructures [68] work at cryogenic temperatures and have very low discrimination (0.4%–5.9%). Circularly polarized light-detecting organic field-effect transistors [69] saturate at very low powers (5 mW/cm^2), operate at very weak currents (nA), and have low quantum efficiency (0.1%). Lead halide perovskites [71,72] present the highest dissymmetry factors and quantum efficiencies, but are for the moment quite difficult to manufacture.

Although the $GaAs_{1-x}N_x$ circular polarimeter itself has not been built yet, based on the available experimental and theoretical results [27–47,49–51,54,55,65] we can say the following. From the data in Figs. 2 and 3, g_d can be estimated to be from 0.8% at low powers to 3.3% at high powers. Recent experimental results on the photoconductivity of a nonoptimized $GaAs_{1-x}N_x$ single

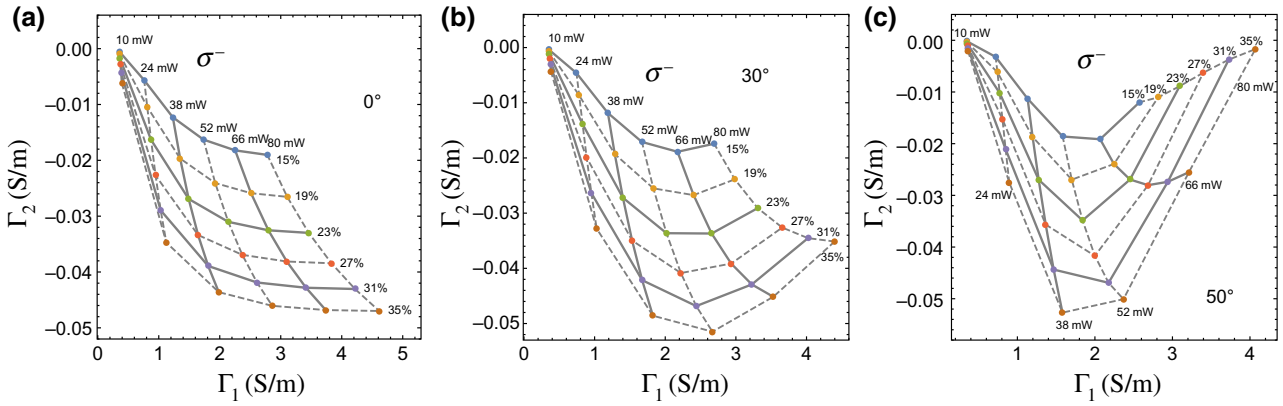

FIG. 5. Power and degree of circular polarization isolines as a function of $\Gamma_1 = \Delta_1(50\text{ mT})$ and $\Gamma_2 = \Delta_2(50\text{ mT})$ under σ^- illumination at relative angles of (a) 0°, (b) 30°, and (c) 50°.

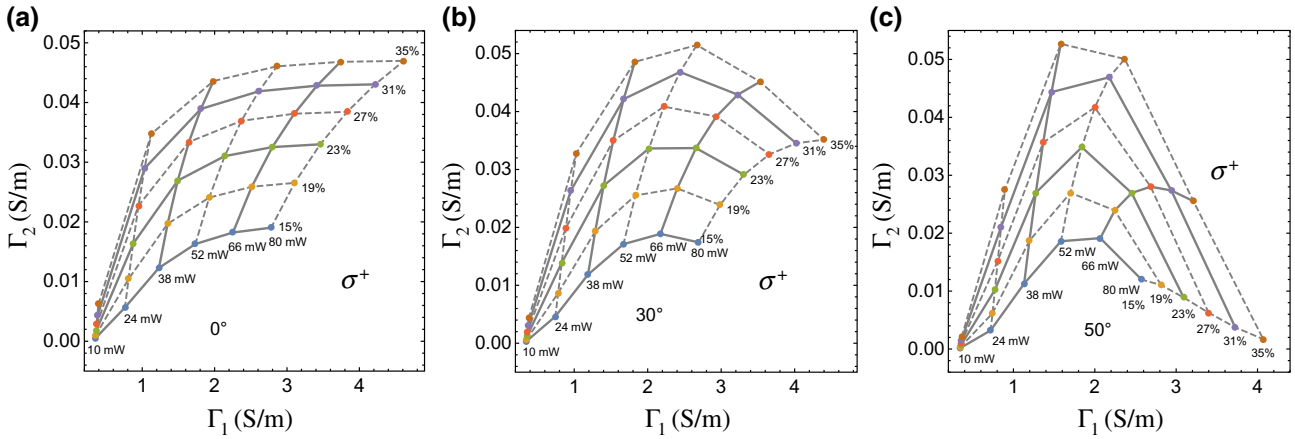

FIG. 6. Power and degree of circular polarization isolines as a function of Γ_1 and Γ_2 under σ^+ illumination at relative angles of (a) 0°, (b) 30°, and (b) 50°.

layer device [65] yield higher dissymmetry factors $g_d = 7.5\%$. $GaAs_{1-x}N_x$ samples have been tested for power densities of up to 40 W/cm^2, yet attaining reasonable discrimination between RHCP and LHCP light at very moderate applied magnetic field values (50 mT) at room temperature. Moreover, it has been shown by us [42,48] that the response of $GaAs_{1-x}N_x$ can be adapted to different power ranges of incident light excitations by optimizing the density of Ga^{2+} centers either by changing the N content [34] or by ion-beam implantation [44]. The spectral range, very wide in III-V materials, can also be readily modulated by the inclusion of defects using any (AlInGa)As alloy to cover from the visible to the telecommunication range (1550 nm). In addition to these features, from Fig. 1 we note that, through the SDR mechanism, linear polarization can also be discriminated. Furthermore, through standard microelectronics techniques $GaAs_{1-x}N_x$ can be easily fabricated as a *p-i-n* diode whose quantum efficiencies typically peak at about 70% [64].

In general, $GaAs_{1-x}N_x$ does not discriminate as well between RHCP and LHCP light as chiral metamaterials, chiral plasmonic devices, chiral $MoSe_2$ metasurfaces, or perovskite-based photodiodes. It can nevertheless maintain reasonable dissymmetry factors while withstanding very high illumination powers. Furthermore, the tolerance to different incidence powers can be tuned by changing the Ga^{2+} concentration as mentioned above. Even though the quantum efficiency of *p-i-n* diodes of similar semiconductors is typically high (70%), this parameter should be evaluated using experimental data from the actual device. In terms of fabrication $GaAs_{1-x}N_x$ is a standard III-V semiconductor material, compatible with traditional microelectronics industry processes and therefore can be fabricated and integrated with ease to standard electronics.

TABLE I. Qualitative and quantitative parameters of circular polarimeters. The table entries that could not be confirmed are left blank. The table entries with a "†" are not directly reported in the corresponding bibliography items, but are determined through the therein reported data.

	Qualitative				Quantitative		
Device	Single shot	Requires off-chip detector	Works at room temperature	Can be integrated to standard electronics	Quantum efficiency (%)	Dissymmetry factor (%)	Saturation power (W/cm^2)
$GaAs_{1-x}N_x$	Yes	No	Yes	Yes	70 [64]	0.3–7.5 [65]	40 [65]
Chiral metamaterials [10,15–17,66,67]		Yes	Yes	Yes	0.2	12.2	
Chiral plasmonic flat devices [14]	Yes	Yes	Yes	Yes		67†	
Chiral $MoSe_2$ metasurface [19]	Yes	No	Yes	Yes		35†	0.05
Photovoltaic spin-Hall [23,24,26]	Yes	No	Yes	Yes			
Silicon-on-insulator [18,21,22]		Yes	Yes	Yes	19		
Fe/MgO/Ge heterostructures [68]			Yes	Yes	2	0.4–5.9	
Organic field-effect transistors [69,70]			No		0.1	5.0	0.005
Perovskite-based photodiode [71,72]		No	Yes	Yes	87.5	185†	

(In, Ga)As quadrant photodiodes are the closest marketed technology to the $GaAs_{1-x}N_x$ polarimeter. These sensors cost between 222 [73], and 1400 USD [74,75]. The design of the $GaAs_{1-x}N_x$ polarimeter contemplates only two active areas and (In, Ga)As four, but each active area also requires a permanent magnet. We can then estimate that the production cost of a quadrant (In, Ga)As would be similar to that of the $GaAs_{1-x}N_x$ circular polarimeter. Hamamatsu, for example, had a gross profit margin of 46.85% [76]; thus, the production cost of such a diode would be roughly 118 USD.

V. CONCLUSIONS

In summary, we have developed the concept of a spin-optoelectronic detector for the simultaneous measurement of the degree of circular polarization, its handedness, and the intensity of a light excitation. We have used a theoretical analysis and numerical simulations based on a master equation approach that has been previously shown to yield very good quantitative agreement with experimental results. The device consists of two independent $GaAs_{1-x}N_x$-based detectors each subject to different magnetic fields generated by small permanent magnets. The values of the magnetic fields are tuned to enhance the sensitivity of each detector to a given property of light. This all-electronic compact device operates at room temperature, requiring no additional bulky movable parts. Ideally, we estimate that, embedded in a *p-i-n* diode, it could operate with high quantum efficiency and dissymmetry factor. The circular polarimeter relies on: (i) the unique spin selection rules of GaAs and spin-dependent capture of CB electrons that takes place through the Ga^{2+} centers in $GaAs_{1-x}N_x$; and (ii) the hyperfine interaction that couples bound electrons and nuclei in the centers and induces an asymmetry in the electron and hole population, making the device sensitive to the circular polarization orientation of the incident light.

We expect that our proposed circular polarimeter will allow for the possibility of simultaneously detecting the intensity and the degree of circular polarization in an integrated optoelectronic platform.

ACKNOWLEDGMENTS

We acknowledge funding from LIA CNRS-Ioffe RAS ILNACS. A.K., J.C.S.S., and V.G.I.S. gratefully appreciate the financial support of the Departamento de Ciencias Básicas UAM-A under Grants No. 2232214 and No. 2232215. X.M. also thanks the Institut Universitaire de France. This work is supported by the Programme Investissements d'Avenir under program ANR-11-IDEX-0002-02, reference ANR-10-LABX-0037-NEXT. E.L.I. is supported by RFBR and CNRS according to research Project No. 20-52-16303.

APPENDIX: MODEL

In this appendix we present a summary of the method used for the computation of the quantum statistical averages of the electron and hole populations $\bar{n}$ and $\bar{p}$, necessary to obtain the conductivity σ_{xx}. For a detailed presentation of this method, see Ref. [63].

Any quantum statistical average may be obtained from the trace of the density matrix multiplied by the appropriate operator. The density matrix ρ, in turn, is ensued from the master equation [63]

$$\frac{d\rho}{dt} = \frac{i}{\hbar}[\rho, H] + \mathcal{D}(\rho), \tag{A1}$$

where H is the Hamiltonian and $\mathcal{D}$ is the dissipator.

The density matrix may be expressed as the direct sum

$$\rho = \rho_v \oplus \rho_c \oplus \rho_1 \oplus \rho_2, \tag{A2}$$

where ρ_v and ρ_c are the density submatrices for valence-band (VB) and conduction-band electrons, respectively. The density submatrices ρ_1 and ρ_2 correspond to singly and doubly occupied Ga^{2+} centers. The density matrix, as any other matrix relevant to Eq. (A1), can be conveniently expanded in terms of the elements of an internal space of Hermitian matrices [63]

$$\begin{aligned}\Lambda &= \{p, S_k, U_{k,j,i}, V_{j,i},\} \\ &= \{\lambda_1, \lambda_2, \ldots, \lambda_d\}, \quad i,j,k = 0,1,2,3,\ d = 85,\end{aligned} \tag{A3}$$

where

$$p = 1_{1\times1} \oplus 0_{2\times2} \oplus 0_{8\times8} \oplus 0_{4\times4}, \tag{A4}$$

$$S_k = 0_{1\times1} \oplus (s_k) \oplus 0_{8\times8} \oplus 0_{4\times4}, \tag{A5}$$

$$U_{k,j,i} = 0_{1\times1} \oplus 0_{2\times2} \oplus (s_k \otimes s_j \otimes s_i) \oplus 0_{4\times4}, \tag{A6}$$

$$V_{j,i} = 0_{1\times1} \oplus 0_{2\times2} \oplus 0_{8\times8} \oplus (s_j \otimes s_i), \tag{A7}$$

with $i,j,k = 0,1,2,3$. Here, $s_0 = 1_{2\times2}/2$, where $1_{2\times2}$ is the 2×2 identity matrix and $s_{1,2,3}$ are the spin matrices following the standard commutation rules

$$[s_i, s_j] = i\hbar \sum_k \epsilon_{i,j,k} s_k, \quad i,j,k = 1,2,3. \tag{A8}$$

This particular choice of a matrix basis is advantageous for a number of reasons. First, any operator can be expressed as a linear combination of the elements of Λ. Second, its elements are orthogonal with respect to the trace,

$$\mathrm{Tr}[\lambda_q^\dagger \lambda_{q'}] = \mathrm{Tr}[\lambda_q^2]\delta_{q,q'}, \tag{A9}$$

which is related to the quantum statistical average of physical observables. Of particular importance are the quantum

statistical averages of the elements of Λ,

$$\bar{\lambda}_q = \mathrm{Tr}[\rho\lambda_q], \tag{A10}$$

whereby the density matrix can be expanded as

$$\rho = \sum_{q=1}^{d} \frac{\bar{\lambda_q}\lambda_q}{\mathrm{Tr}[\lambda_q^2]} = \frac{\bar{p}p}{\mathrm{Tr}[p^2]} + \sum_{k=0}^{3} \frac{\bar{S}_k S_k}{\mathrm{Tr}[S_k^2]} + \sum_{k,j,i=0}^{3} \frac{\bar{U}_{k,j,i}U_{k,j,i}}{\mathrm{Tr}[U_{k,j,i}^2]} + \sum_{j,i=0}^{3} \frac{\bar{V}_{j,i}V_{j,i}}{\mathrm{Tr}[V_{j,i}^2]}. \tag{A11}$$

Any operator O can be expanded in this basis as

$$O = \sum_{q=1}^{d} \frac{\mathrm{Tr}[O\lambda_q]}{\mathrm{Tr}[\lambda_q^2]}\lambda_q = \frac{\mathrm{Tr}[Op]p}{\mathrm{Tr}[p^2]} + \sum_{k=0}^{3} \frac{\mathrm{Tr}[OS_k]S_k}{\mathrm{Tr}[S_k^2]} + \sum_{k,j,i=0}^{3} \frac{\mathrm{Tr}[OU_{k,j,i}]U_{k,j,i}}{\mathrm{Tr}[U_{k,j,i}^2]} + \sum_{j,i=0}^{3} \frac{\mathrm{Tr}[OV_{j,i}]V_{j,i}}{\mathrm{Tr}[V_{j,i}^2]}, \tag{A12}$$

and its corresponding quantum statistical average is given by

$$\bar{O} = \mathrm{Tr}[O\rho] = \sum_{q=1}^{d} \frac{\mathrm{Tr}[O\lambda_q]}{\mathrm{Tr}[\lambda_q^2]}\bar{\lambda}_q. \tag{A13}$$

In this way, the density of VB holes is represented by the matrix p, the density of CB electrons by $n = 2S_0$, the spin components of CB electrons by S_k $(k = 1, 2, 3)$, the concentration of singly occupied traps by $N_1 = 8U_{0,0,0}$, the spin components of bound electrons in Ga^{2+} centers by $S_{ck} = 4U_{k,0,0}$ $(k = 1, 2, 3)$, and the concentration of doubly occupied traps by $N_2 = 4V_{0,0}$. Using Eq. (A12), we can also decompose more complicated operators. For instance, the components of the nuclear spin operators of singly charged centers $\mathbf{I}_1$ and doubly charged centers $\mathbf{I}_2$ can readily be expressed as a superposition of the elements of Eq. (A3) by

$$I_{1,k} = \sum_{j,i=0}^{3} \frac{\mathrm{Tr}[I_{1,k}U_{0,j,i}]}{\mathrm{Tr}[U_{0,j,i}U_{0,j,i}]}U_{0,j,i}, \tag{A14}$$

$$I_{2,k} = \sum_{j,i=0}^{3} \frac{\mathrm{Tr}[I_{2,k}V_{j,i}]}{\mathrm{Tr}[V_{j,i}V_{j,i}]}V_{j,i}. \tag{A15}$$

Note that in the previous expressions only a few elements of the basis are needed.

The Hamiltonian in Eq. (A1),

$$H = \hbar\boldsymbol{\omega}\cdot\mathbf{S} + \hbar\boldsymbol{\Omega}\cdot\mathbf{S}_c + A\mathbf{I}_1\cdot\mathbf{S}_c, \tag{A16}$$

accounts for the Zeeman and hyperfine interactions. The first two terms correspond to the Zeeman interaction of an external magnetic field $\mathbf{B}$ with the CB electron spin $\mathbf{S}$ and the center's bound electron spin $\mathbf{S}_c$. In these expressions $\boldsymbol{\omega} = g\mu_B\mathbf{B}/\hbar$, $\boldsymbol{\Omega} = g_c\mu_B\mathbf{B}/\hbar$, where μ_B is the Bohr magneton, g is the gyromagnetic factor for CB electrons, and $g_c = 2$ [51] is the gyromagnetic factor for bound electrons in singly occupied centers. The third term is responsible for the hyperfine interaction that takes place in singly occupied centers between the bound electron spin $\mathbf{S}_c$ and the nuclear spin $\mathbf{I}_1$. The hyperfine parameter is A. In doubly occupied traps electrons form a singlet state that does not interact with the nuclear spin $\mathbf{I}_2$.

The dissipator

$$\mathcal{D}(\rho) = \mathcal{G} + \mathcal{D}_S + \mathcal{D}_{\mathrm{SC}} + \mathcal{D}_1 + \mathcal{D}_2 + \mathcal{D}_{\mathrm{SDR}} + \mathcal{D}_P \tag{A17}$$

is primarily composed of generation ($\mathcal{G}$), spin relaxation ($\mathcal{D}_S$ and $\mathcal{D}_{\mathrm{SC}}$, $\mathcal{D}_1$ and $\mathcal{D}_2$), and recombination terms ($\mathcal{D}_{\mathrm{SDR}}$ and $\mathcal{D}_P$) The electron-hole pair generating term is given by

$$\mathcal{G} = (G_+ + G_-)(p + n) + 2(G_+ - G_-)\mathbf{e}\cdot\mathbf{S}, \tag{A18}$$

where $\mathbf{e}$ is a unitary vector in the excitation direction. Spin-up and spin-down CB electron generation rates are given by the smooth step function

$$G(t)_\pm = \frac{G_0 P_{\mathrm{exc}}}{2}\frac{1 \pm P_e}{2}\left[1 + \tanh\left(\frac{t - t_0}{\Delta t}\right)\right], \tag{A19}$$

where P_{exc} is the excitation power, G_0 is the power to generation factor, Δt is the width of the step function, and the spin polarization degree is parameterized by $P_e \in [-1, 1]$.

The electronic and nuclear spin relaxation dissipators are derived from Wangsness-Bloch-Redfield theory [51, 77–79]. The dissipator for CB electrons straightforwardly gives

$$\mathcal{D}_S = -\frac{1}{2\tau_s}\sum_{k=1}^{3}[S_k, [S_k, \rho]]. \tag{A20}$$

The spin relaxation dissipators in centers require closer attention. Following the same line as Ref. [51], we consider that in singly and doubly occupied traps the dipole-dipole interaction between centers and neighboring Ga atoms is the leading mechanism of nuclear spin relaxation. Here, however, we distinguish between three different relaxation times associated with the electron-nucleus states of singly occupied traps, in contrast to our previous models

[51,63], where only two were used. Apart from the preexisting relaxation times τ_{sc} for bound electron spin states and τ_{n1} for nuclear spin states we add the relaxation time τ_{co} for electron-nucleus spin correlations. This considerably improves the agreement between the experimental and theoretical results because, as the fit of the model through experimental data shows, the spin relaxation of correlations ($\tau_{co} = 8$ ns) is at least 4 times slower than the electronic or nuclear spin relaxation times ($\tau_{sc} = 2$ ns and $\tau_{n1} = 2$ ns). In earlier approaches the value of τ_{co} was tied to the values of τ_{sc} and τ_{n1}, forcing the system to unrealistically small electron-nucleus spin correlation relaxation times. This improvement is particularly clear in the plot for the photoluminescence as a function of the applied magnetic field tilted from a Faraday to Voigt configuration, as can be seen in Fig. 7. In this figure we show a comparison between the experimental data [panel (a)] and the theoretical results produced by the model [panel (b)] for the photoluminescence for various magnetic field directions. These curves are particularly sensitive to the spin relaxation times since, as the magnetic field direction changes, different spin relaxation times come into play. A similar plot can be found in Ref. [63], which confirms that the curve widths in Voigt and Faraday configurations show better consistency with the experimental results when τ_{co} is introduced into the model. This improvement is essential to get reliable quantitative predictions on the performance of the device.

To separate the relaxation times of pure spins from electron-nucleus spin correlations, we break the dissipator of the singly occupied centers into three parts through projection on the following subbasis of Λ: $U_{k,0,0}$ with $k = 1,2,3$ for bound electron spins, $U_{0,j,i}$ with $i,j = 1,2,3$ or $i = 0$ and $j = 1,2,3$ or $j = 0$ and $i = 1,2,3$ for nuclear spins, and $U_{k,j,i}$ with $i,j,k = 1,2,3$ or $i = 0$ and $j,k = 1,2,3$ or $j = 0$ and $i,k = 1,2,3$ for electron-nucleus spin correlations.

The dissipator for the bound electron spin can thus be expanded in terms of the Λ elements corresponding to the singly occupied traps

$$\mathcal{D}_{SC} = -\frac{1}{2\tau_{sc}} \sum_{k=1}^{3} \frac{\mathrm{Tr}[\Gamma_S U_{k,0,0}]}{\mathrm{Tr}[U_{k,0,0} U_{k,0,0}]} U_{k,0,0} - \frac{1}{2\tau_{co}} \sum_{k,j,i=0}^{3} \mu_{k,j,i} \frac{\mathrm{Tr}[\Gamma_S U_{k,j,i}]}{\mathrm{Tr}[U_{k,j,i} U_{k,j,i}]} U_{k,j,i}, \quad \text{(A21)}$$

where

$$\Gamma_S = \sum_{k=1}^{3} [S_{ck}, [S_{ck}, \rho]] \quad \text{(A22)}$$

is the usual commutator arising from Wangsness-Bloch-Redfield theory for dipole-dipole interaction. The first term of Eq. (A21) is the projection of Γ_S on to the electron spin subbasis of Λ, namely, the spin components of the bound electron $S_{ck} = 4U_{k,0,0}$ for $k = 1,2,3$. Accordingly, the second term of Eq. (A21) is the projection of Γ_S on to the subbasis of electron-nucleus correlations, which are selected by

$$\mu_{k,j,i} = \begin{cases} 0, & k = 0 \vee (k \neq 0 \wedge j = 0 \wedge i = 0), \\ 1, & k \neq 0 \wedge (j \neq 0 \vee i \neq 0). \end{cases} \quad \text{(A23)}$$

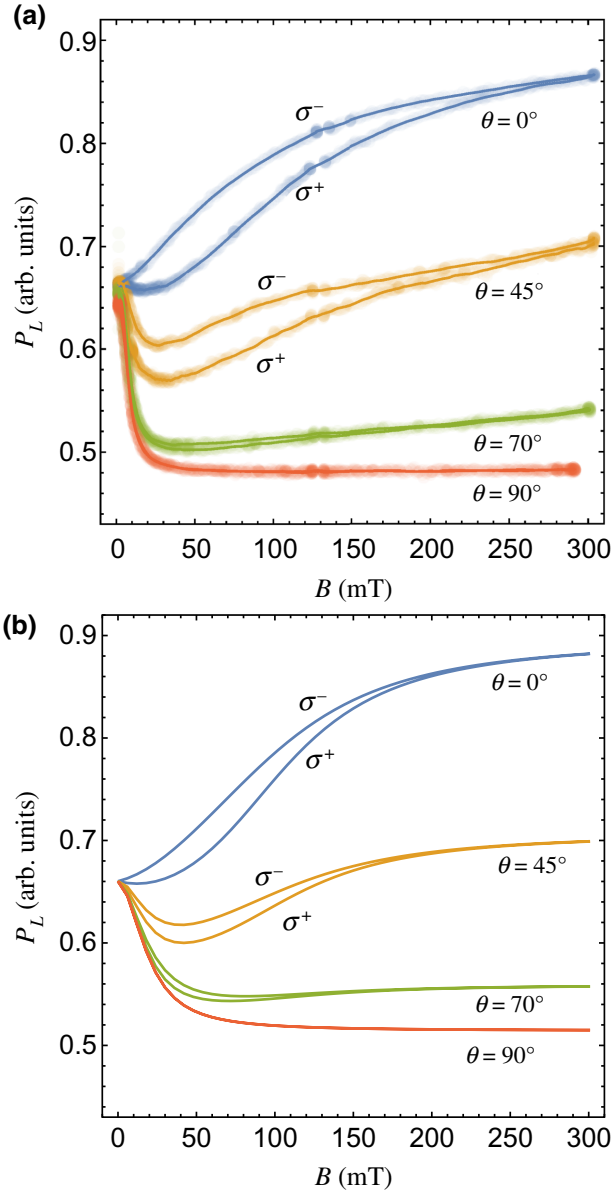

FIG. 7. (a) Experimental and (b) theoretical results for the photoluminescence P_L as a function of an oblique magnetic field at an incident power of 20 mW. The magnetic field is rotated from a Faraday ($\theta = 0°$) to Voight ($\theta = 90°$) configuration. In panel (a) the dots correspond to the experimental results and the solid lines are a guide to the eye.

As discussed above, each of these projections is governed by a different relaxation time: τ_{sc} is the electronic spin relaxation time and τ_{co} is the relaxation time of correlations in singly occupied traps. Similarly, the nuclear spin relaxation dissipator is expanded as

$$\mathcal{D}_1 = -\frac{1}{3\tau_{n1}}\sum_{k=1}^{3}\frac{\mathrm{Tr}[\Gamma_I U_{k,0,0}]}{\mathrm{Tr}[U_{k,0,0}U_{k,0,0}]}U_{k,0,0} - \frac{1}{2\tau_{co}}\sum_{k,j,i=0}^{3}\mu_{k,j,i}\frac{\mathrm{Tr}[\Gamma_I U_{k,j,i}]}{\mathrm{Tr}[U_{k,j,i}U_{k,j,i}]}U_{k,j,i}, \quad \text{(A24)}$$

where

$$\Gamma_I = \sum_{k=1}^{3}[I_{1k},[I_{1k},\rho]] \quad \text{(A25)}$$

comes out of the dipole-dipole interaction between the center's nuclear spin and the neighboring Ga nuclei. In the equations above the nuclear spin relaxation time in singly occupied traps is τ_{n1}. Note that the electron-nucleus spin correlation relaxation time τ_{co} newly appears in this dissipator.

The dissipator of doubly occupied centers reads

$$\mathcal{D}_2 = -\frac{1}{3\tau_{n2}}\sum_{k=1}^{3}[I_{2k},[I_{2k},\rho]], \quad \text{(A26)}$$

where τ_{n2} is the corresponding nuclear spin relaxation time. Since in doubly occupied centers both electrons residing in the $4s$ orbital form a singlet state that is not correlated to the nuclear spin, $\mathcal{D}_2$ does not need to be separated into the spin and correlation parts.

The spin-selective capture of electrons into singly occupied centers is accounted for by the dissipator [63]

$$\mathcal{D}_{SDR} = -2\sum_{k=0}^{3}\left(4c_n\sum_{k',k''=0}^{3}\bar{S}_{k'}Q^{\top}_{k,k',k''}\bar{U}_{k'',j,i}\right)S_k - 8\sum_{k,j,i=0}^{3}\mu_{k,j,i}I\left(c_n\sum_{k',k''=0}^{3}\bar{S}_{k'}Q_{k,k',k''}\bar{U}_{k'',j,i}\right)U_{k,j,i} + 4\sum_{j,i=0}^{3}\left(2c_n\sum_{k',k''=0}^{3}\bar{S}_{k'}Q^{\top}_{0,k',k''}\bar{U}_{k'',j,i}\right)V_{j,i}, \quad \text{(A27)}$$

where the capture coefficient of CB electrons $c_n = 1/N_0\tau^*$, τ^* is the electron recombination time in the low excitation power regime, and N_0 is the total number of centers in the sample. The matrices $Q_{k,k',k''} = (\mathbb{Q}_k)_{k',k''}$, related to the space rotation generators [80], are responsible for the spin-dependent capture. These are defined by

$$\mathbb{Q}_0 = \begin{pmatrix}1&0&0&0\\0&-1&0&0\\0&0&-1&0\\0&0&0&-1\end{pmatrix}, \quad \mathbb{Q}_1 = \begin{pmatrix}0&1&0&0\\-1&0&0&0\\0&0&0&0\\0&0&0&0\end{pmatrix},$$
$$\mathbb{Q}_2 = \begin{pmatrix}0&0&1&0\\0&0&0&0\\-1&0&0&0\\0&0&0&0\end{pmatrix}, \quad \mathbb{Q}_3 = \begin{pmatrix}0&0&0&1\\0&0&0&0\\0&0&0&0\\-1&0&0&0\end{pmatrix}. \quad \text{(A28)}$$

Note that, while $\mathbb{Q}_0$ remains invariant under rotations, $\mathbb{Q}_1$, $\mathbb{Q}_2$, and $\mathbb{Q}_3$ rotate as the components of a three-dimensional vector.

The recombination of VB holes into doubly occupied centers is governed by the dissipator [63]

$$\mathcal{D}_P = -(4c_p\bar{p}\,\bar{V}_{0,0})p + \frac{1}{8}\left(\frac{1}{2}\sum_{j,i=0}^{3}\bar{p}\,\bar{V}_{j,i}\right)U_{0,j,i} - \frac{1}{4}\left(\sum_{j,i=0}^{3}\bar{p}\,\bar{V}_{j,i}\right)V_{j,i}, \quad \text{(A29)}$$

where $c_p = 1/N_0\tau_h$ is the capture coefficient for holes and τ_h is the hole recombination time in the high excitation power regime.

Having established the components of the master equation, we now turn our attention to the determination of the time dependence of observables such as $\bar{n}$ and $\bar{p}$. Instead of directly solving the system of ordinary differential equations arising from Eq. (A1) for the matrix elements of ρ, we determine the system of ordinary differential equations for the statistical averages of the elements of Λ. This procedure yields $d = 85$ differential equations of the form

$$\frac{d\bar{\lambda}_q}{dt} = \frac{i}{\hbar}\mathrm{Tr}[[H,\lambda_q]\rho] + \mathrm{Tr}[\mathcal{D}(\rho)\lambda_q]. \quad \text{(A30)}$$

These are solved numerically over a sufficiently long time (approximately 400 ns) to allow steady-state conditions to be reached. Finally, the quantum average of any operator can be computed from decomposition (A13). In particular, the CB electron and VB hole densities are

$$\bar{n} = \sum_{q=1}^{d}\frac{\mathrm{Tr}[n\lambda_q]}{\mathrm{Tr}[\lambda_q^2]}\bar{\lambda}_q, \quad \text{(A31)}$$

$$\bar{p} = \sum_{q=1}^{d}\frac{\mathrm{Tr}[p\lambda_q]}{\mathrm{Tr}[\lambda_q^2]}\bar{\lambda}_q. \quad \text{(A32)}$$

In order for the model to yield quantitatively realistic results, we have fitted its parameters using experimental measurements of the photoluminescence for various

incident powers and magnetic field orientations. Varying the magnetic field orientation provides a complete set of experimental points, especially useful to determine the electronic and nuclear spin relaxation times τ_h, τ_r, τ^*, τ_s, τ_{sc}, τ_{sco}, τ_{n1}, τ_{n1co}, and τ_{n2}. The photoluminescence, on the other hand, yields information on the power to generation factor G_0 and the overall number of paramagnetic centers $N_c = N_1 + N_2$ in the sample. The photoluminescence measurements are performed on a 100 nm thick $GaAs_{1-x}N_x$ epilayer ($x = 0.021$) grown by molecular beam epitaxy on a (001) semi-insulating GaAs substrate and capped with 10 nm GaAs. The room-temperature epilayer gap is 1080 nm. The excitation light is provided by a 850 nm laser diode. The model is fitted using the experimental data of the photoluminescence as a function of the magnetic field taken at incident powers starting at 20 mW (shown in Fig. 7) going up to 80 mW (not shown here). The parameters that best fit the experimental results on photoluminescence are $G_0 = 3 \times 10^{23}\ \mathrm{cm^{-3}\,mW^{-1}}$, $\Delta t = 10$ ps, $N_c = N_1 + N_2 = 2.2 \times 10^{15}\ \mathrm{cm^{-3}}$, $\tau_h = 20$ ps, $\tau_r = 1.4$ ns, $\tau^* = 10$ ps, $\tau_s = 120$ ps, $\tau_{sc} = 2$ ns, $\tau_{co} = 8$ ns, $\tau_{n1} = 2$ ns, $\tau_{n2} = 100$ ps, $A = 0.069\ \mathrm{cm^{-1}}$ [46], $g = 1$, and $g_c = 2$ [51,63].

[1] W. B. Sparks, T. A. Germer, and R. M. Sparks, Classical polarimetry with a twist: A compact, geometric approach, Publ. Astron. Soc. Pac. **131**, 075002 (2019).

[2] P. Whittaker, R. A. Kloner, D. R. Boughner, and J. G. Pickering, Quantitative assessment of myocardial collagen with picrosirius red staining and circularly polarized light, Basic Res. Cardiol. **89**, 397 (1994).

[3] D. C. Louie, L. Tchvialeva, S. Kalia, H. Lui, and T. K. Lee, in *Dermatology and Plastic Surgery 2018*, edited by B. Choiand and H. Zeng (SPIE, San Francisco, California, USA, 2018), Vol. 10467, p. 44.

[4] J. Chang, H. He, Y. Wang, Y. Huang, X. Li, C. He, R. Liao, N. Zeng, S. Liu, and H. Ma, Division of focal plane polarimeter-based 3 × 4 Mueller matrix microscope: A potential tool for quick diagnosis of human carcinoma tissues, J. Biomed. Opt. **21**, 1 (2016).

[5] W. B. Gao, P. Fallahi, E. Togan, J. Miguel-Sanchez, and A. Imamoglu, Observation of entanglement between a quantum dot spin and a single photon, Nature **491**, 426 (2012).

[6] M. K. Bhaskar, R. Riedinger, B. Machielse, D. S. Levonian, C. T. Nguyen, E. N. Knall, H. Park, D. Englund, M. Lončar, D. D. Sukachev, and M. D. Lukin, Experimental demonstration of memory-enhanced quantum communication, Nature **580**, 60 (2020).

[7] E. Togan, Y. Chu, A. S. Trifonov, L. Jiang, J. Maze, L. Childress, M. V. G. Dutt, A. S. Sørensen, P. R. Hemmer, A. S. Zibrov, and M. D. Lukin, Quantum entanglement between an optical photon and a solid-state spin qubit, Nature **466**, 730 (2010).

[8] D. D. B. Rao, S. Yang, and J. Wrachtrup, Generation of entangled photon strings using NV centers in diamond, Phys. Rev. B **92**, 081301 (2015).

[9] H. G. Berry, G. Gabrielse, and A. E. Livingston, Measurement of the stokes parameters of light, Appl. Opt. **16**, 3200 (1977).

[10] A. Basiri, X. Chen, J. Bai, P. Amrollahi, J. Carpenter, Z. Holman, C. Wang, and Y. Yao, Nature-inspired chiral metasurfaces for circular polarization detection and full-stokes polarimetric measurements, Light: Sci. Appl. **8**, 78 (2019).

[11] O. Awartani, M. W. Kudenov, and B. T. O'Connor, Organic photovoltaic cells with controlled polarization sensitivity, Appl. Phys. Lett. **104**, 093306 (2014).

[12] S. G. Roy, O. M. Awartani, P. Sen, B. O'Connor, and M. W. Kudenov, Intrinsic coincident linear polarimetry using stacked organic photovoltaics, Opt. Express **24**, 14737 (2016).

[13] R. Yang, P. Sen, B. T. O'Connor, and M. W. Kudenov, Intrinsic coincident full-stokes polarimeter using stacked organic photovoltaics, Appl. Opt. **56**, 1768 (2017).

[14] J. Bai, C. Wang, X. Chen, A. Basiri, C. Wang, and Y. Yao, Chip-integrated plasmonic flat optics for mid-infrared full-stokes polarization detection, Photonics Res. **7**, 1051 (2019).

[15] M. Akbari, J. Gao, and X. Yang, Generation of transverse photo-induced voltage in plasmonic metasurfaces of triangle holes, Opt. Express **26**, 21194 (2018).

[16] J. Hu, X. Zhao, Y. Lin, A. Zhu, X. Zhu, P. Guo, B. Cao, and C. Wang, All-dielectric metasurface circular dichroism waveplate, Sci. Rep. **7**, 41893 (2017).

[17] Y. Zhao, M. A. Belkin, and A. Alù, Twisted optical metamaterials for planarized ultrathin broadband circular polarizers, Nat. Commun. **3**, 870 (2012).

[18] Z. Lin, L. Rusch, Y. Chen, and W. Shi, Chip-scale, full-stokes polarimeter, Opt. Express **27**, 4867 (2019).

[19] Q. Jiang, B. Du, M. Jiang, D. Liu, Z. Liu, B. Li, Z. Liu, F. Lin, X. Zhu, and Z. Fang, Ultrathin circular polarimeter based on chiral plasmonic metasurface and monolayer $MoSe_2$, Nanoscale **12**, 5906 (2020).

[20] L. P. Stoevelaar, J. Berzinš, F. Silvestri, S. Fasold, K. Z. Kamali, H. Knopf, F. Eilenberger, F. Setzpfandt, T. Pertsch, S. M. B. Bäumer, and G. Gerini, Nanostructure-modulated planar high spectral resolution spectro-polarimeter, Opt. Express **28**, 19818 (2020).

[21] W. Wu, Y. Yu, W. Liu, and X. Zhang, Fully integrated CMOS-compatible polarization analyzer, Nanophotonics **8**, 467 (2019).

[22] J. Dong and H. Zhou, Polarimeters from bulky optics to integrated optics: A review, Opt. Commun. **465**, 125598 (2020).

[23] K. Ando, M. Morikawa, T. Trypiniotis, Y. Fujikawa, C. H. W. Barnes, and E. Saitoh, Photoinduced inverse spin-hall effect: Conversion of light-polarization information into electric voltage, Appl. Phys. Lett. **96**, 082502 (2010).

[24] S. K. Khamari, S. Porwal, S. M. Oak, and T. K. Sharma, A spin-optoelectronic detector for the simultaneous measurement of the degree of circular polarization and intensity of a laser beam, Appl. Phys. Lett. **107**, 072108 (2015).

[25] E. L. Ivchenko and S. D. Ganichev, Spin-dependent photogalvanic effects (a review), ArXiv:1710.09223 (2017).

[26] E. Saitoh, M. Ueda, H. Miyajima, and G. Tatara, Conversion of spin current into charge current at room temperature: Inverse spin-hall effect, Appl. Phys. Lett. **88**, 182509 (2006).

[27] D. J. Lepine, Spin-dependent recombination on silicon surface, Phys. Rev. B **6**, 436 (1972).

[28] C. Weisbuch and G. Lampel, Spin-dependent recombination and optical spin orientation in semiconductors, Solid State Commun. **14**, 141 (1974).

[29] D. Paget, Optical-pumping study of spin-dependent recombination in GaAs, Phys. Rev. B **30**, 931 (1984).

[30] V. K. Kalevich, E. L. Ivchenko, M. M. Afanasiev, A. Y. Shiryaev, A. Y. Egorov, V. M. Ustinov, B. Pal, and Y. Masumoto, Spin-dependent recombination in (Ga, As)N solid solutions, J. Exp. Theor. Phys. Lett. **82**, 455 (2005).

[31] L. Lombez, P.-F. Braun, H. Carrère, B. Urbaszek, P. Renucci, T. Amand, X. Marie, J. C. Harmand, and V. K. Kalevich, Spin dynamics in dilute nitride semiconductors at room temperature, Appl. Phys. Lett. **87**, 252115 (2005).

[32] V. K. Kalevich, A. Y. Shiryaev, E. L. Ivchenko, A. Y. Egorov, L. Lombez, D. Lagarde, X. Marie, and T. Amand, Spin-dependent electron dynamics and recombination in $GaAs_{1-x}N_x$ alloys at room temperature, JETP Lett. **85**, 174 (2006).

[33] D. Lagarde, L. Lombez, X. Marie, A. Balocchi, T. Amand, V. K. Kalevich, A. Shiryaev, E. Ivchenko, and A. Egorov, Electron spin dynamics in (Ga, As)N and InGaAsN structures, Phys. Status Solidi (a) **204**, 208 (2007).

[34] F. Zhao, A. Balocchi, G. Truong, T. Amand, X. Marie, X. J. Wang, I. A. Buyanova, W. M. Chen, and J. C. Harmand, Electron spin control in dilute nitride semiconductors, J. Phys.: Condens. Matter **21**, 174211 (2009).

[35] X. J. Wang, I. A. Buyanova, F. Zhao, D. Lagarde, A. Balocchi, X. Marie, C. W. Tu, J. C. Harmand, and W. M. Chen, Room-temperature defect-engineered spin filter based on a non-magnetic semiconductor, Nat. Mater. **8**, 198 (2009).

[36] V. Kalevich, A. Shiryaev, E. Ivchenko, M. Afanasiev, A. Egorov, V. Ustinov, and Y. Masumoto, Hanle effect and spin-dependent recombination at deep centers in (Ga, As)N, Phys. B: Condens. Matter **404**, 4929 (2009).

[37] H. M. Zhao, L. Lombez, B. L. Liu, B. Q. Sun, Q. K. Xue, D. M. Chen, and X. Marie, Electron spin quantum beats and room temperature g factor in (Ga, As)N, Appl. Phys. Lett. **95**, 041911 (2009).

[38] F. Zhao, A. Balocchi, A. Kunold, J. Carrey, H. Caré, T. Amand, N. Ben Abdallah, J. C. Harmand, and X. Marie, Spin-dependent photoconductivity in nonmagnetic semiconductors at room temperature, Appl. Phys. Lett. **95**, 241104 (2009).

[39] X. J. Wang, Y. Puttisong, C. W. Tu, A. J. Ptak, V. K. Kalevich, A. Y. Egorov, L. Geelhaar, H. Riechert, W. M. Chen, and I. A. Buyanova, Dominant recombination centers in Ga(In)NAs alloys: Ga interstitials, Appl. Phys. Lett. **95**, 241904 (2009).

[40] Y. Puttisong, X. J. Wang, I. A. Buyanova, H. Carrère, F. Zhao, A. Balocchi, X. Marie, C. W. Tu, and W. M. Chen, Electron spin filtering by thin GaNAs/GaAs multiquantum wells, Appl. Phys. Lett. **96**, 052104 (2010).

[41] E. L. Ivchenko, V. K. Kalevich, A. Y. Shiryaev, M. M. Afanasiev, and Y. Masumoto, Optical orientation and spin-dependent recombination in (Ga, As)N alloys under continuous-wave pumping, J. Phys.: Condens. Matter **22**, 465804 (2010).

[42] A. Kunold, A. Balocchi, F. Zhao, T. Amand, N. B. Abdallah, J. C. Harmand, and X. Marie, Giant spin-dependent photo-conductivity in (Ga, As)N dilute nitride semiconductor, Phys. Rev. B **83**, 165202 (2011).

[43] V. K. Kalevich, M. M. Afanasiev, A. Y. Shiryaev, and A. Y. Egorov, Amplification of spin-filtering effect by magnetic field in (Ga, As)N alloys, Phys. Rev. B **85**, 035205 (2012).

[44] C. T. Nguyen, A. Balocchi, D. Lagarde, T. T. Zhang, H. Carrère, S. Mazzucato, P. Barate, E. Galopin, J. Gierak, E. Bourhis, J. C. Harmand, T. Amand, and X. Marie, Fabrication of an (In, Ga)As spin filter by implantation of paramagnetic centers, Appl. Phys. Lett. **103**, 052403 (2013).

[45] V. K. Kalevich, M. M. Afanasiev, A. Y. Shiryaev, and A. Y. Egorov, Optical orientation of nuclei in nitrogen alloys (Ga, As)N at room temperature, JETP Lett. **96**, 567 (2013).

[46] Y. Puttisong, X. J. Wang, I. A. Buyanova, L. Geelhaar, H. Riechert, A. J. Ptak, C. W. Tu, and W. M. Chen, Efficient room-temperature nuclear spin hyperpolarization of a defect atom in a semiconductor, Nat. Commun. **4**, 1751 (2013).

[47] Y. Puttisong, X. J. Wang, I. A. Buyanova, and W. M. Chen, Effect of hyperfine-induced spin mixing on the defect-enabled spin blockade and spin filtering in GaNAs, Phys. Rev. B **87**, 125202 (2013).

[48] C. Sandoval-Santana, A. Balocchi, T. Amand, J. C. Harmand, A. Kunold, and X. Marie, Room-temperature optical manipulation of nuclear spin polarization in (Ga, As)N, Phys. Rev. B **90**, 115205 (2014).

[49] E. L. Ivchenko, L. A. Bakaleinikov, and V. K. Kalevich, Spin-dependent recombination and hyperfine interaction at deep defects, Phys. Rev. B **91**, 205202 (2015).

[50] E. L. Ivchenko, L. A. Bakaleinikov, M. M. Afanasiev, and V. K. Kalevich, Spin-dependent recombination in $GaAs_{1-x}N_x$ alloys at oblique magnetic field, Phys. Solid State **58**, 1539 (2016).

[51] V. G. Ibarra-Sierra, J. C. Sandoval-Santana, S. Azaizia, H. Carrère, L. A. Bakaleinikov, V. K. Kalevich, E. L. Ivchenko, X. Marie, T. Amand, A. Balocchi, and A. Kunold, Electron-nuclear spin dynamics of Ga^2+ paramagnetic centers probed by spin-dependent recombination: A master equation approach, Phys. Rev. B **95**, 195204 (2017).

[52] S. Azaizia, H. Carrère, J. C. Sandoval-Santana, V. G. Ibarra-Sierra, V. K. Kalevich, E. L. Ivchenko, L. A. Bakaleinikov, X. Marie, T. Amand, A. Kunold, and A. Balocchi, Electron-nuclear coherent spin oscillations probed by spin-dependent recombination, Phys. Rev. B **97**, 155201 (2018).

[53] J. C. Sandoval-Santana, V. G. Ibarra-Sierra, S. Azaizia, H. Carrère, L. A. Bakaleinikov, V. K. Kalevich, E. L. Ivchenko, X. Marie, T. Amand, A. Balocchi, and A. Kunold, Electron-nuclear spin dynamics of Ga centers in (Ga, As)N dilute nitride semiconductors probed by pump-probe spectroscopy, Eur. Phys. J. Plus **133**, 122 (2018).

[54] V. G. Ibarra-Sierra, J. C. Sandoval-Santana, S. Azaizia, H. Carrère, L. A. Bakaleinikov, V. K. Kalevich, E. L. Ivchenko, X. Marie, T. Amand, A. Balocchi, and A. Kunold, Spin-filtering effect in (Ga, As)N: Electron-nuclear spin dynamics of Ga^{3+} centers, J. Mater. Sci.: Mater. Electron. **29**, 15307 (2018).

[55] S. Chen, Y. Huang, D. Visser, S. Anand, I. A. Buyanova, and W. M. Chen, Room-temperature polarized spin-photon interface based on a semiconductor nanodisk-in-nanopillar

structure driven by few defects, Nat. Commun. **9**, 3575 (2018).
[56] F. Meier and B. P. Zakharchenya, *Optical Orientation* (Elsevier, Amsterdam, The Netherlands, 1984).
[57] M. Reason, Y. Jin, H. A. McKay, N. Mangan, D. Mao, R. S. Goldman, X. Bai, and C. Kurdak, Influence of N on the electronic properties of (Ga, As)N alloy films and heterostructures, J. Appl. Phys. **102**, 103710 (2007).
[58] S. Dhar, A. Mondal, and T. D. Das, Hall mobility and electron trap density in (Ga, As)N grown by liquid phase epitaxy, Semicond. Sci. Technol. **23**, 015007 (2007).
[59] J. Ibáñez, R. Cuscó, E. Alarcón-Lladó, L. Artús, A. Patanè, D. Fowler, L. Eaves, K. Uesugi, and I. Suemune, Electron effective mass and mobility in heavily doped *n*-(Ga, As)N probed by raman scattering, J. Appl. Phys. **103**, 103528 (2008).
[60] H. Suzuki, T. Hashiguchi, N. Kojima, Y. Ohshita, and M. Yamaguchi, in *2009 34th IEEE Photovoltaic Specialists Conference* (PVSC, IEEE, Philadelphia, Pennsylvania, 2009), p. 1140.
[61] M. Inagaki, K. Ikeda, H. Kowaki, Y. Ohshita, N. Kojima, and M. Yamagichi, Dominant mechanisms of electron scattering in ultra-dilute (Ga, As)N, Phys. Status Solidi (c) **10**, 589 (2013).
[62] A. Patanè, G. Allison, L. Eaves, M. Hopkinson, G. Hill, and A. Ignatov, Tailoring the electrical conductivity of GaAs by nitrogen incorporation, J. Phys.: Condens. Matter **21**, 174209 (2009).
[63] J. C. Sandoval-Santana, V. G. Ibarra-Sierra, H. Carrère, M. M. Afanasiev, L. A. Bakaleinikov, V. K. Kalevich, E. L. Ivchenko, X. Marie, T. Amand, A. Balocchi, and A. Kunold, Electron-nucleus spin-correlation conservation of spin-dependent recombination in Ga^{2+} centers, Phys. Rev. B **101**, 075201 (2020).
[64] J. Campbell, A. Dentai, G. Qua, J. Long, and V. Riggs, Planar (In, Ga)As pin photodiode with a semi-insulating InP cap layer, Electron. Lett. **21**, 447 (1985).
[65] R. S. Joshya, H. Carrère, V. G. Ibarra-Sierra, J. C. Sandoval-Santana, V. K. Kalevich, E. L. Ivchenko, X. Marie, T. Amand, A. Kunold, and A. Balocchi, Chiral photodetector based on GaAsN, Adv. Funct. Mater., 2102003 (2021).
[66] A. Sobhani, M. W. Knight, Y. Wang, B. Zheng, N. S. King, L. V. Brown, Z. Fang, P. Nordlander, and N. J. Halas, Narrowband photodetection in the near-infrared with a plasmon-induced hot electron device, Nat. Commun. **4**, 1643 (2013).
[67] W. Li, Z. J. Coppens, L. V. Besteiro, W. Wang, A. O. Govorov, and J. Valentine, Circularly polarized light detection with hot electrons in chiral plasmonic metamaterials, Nat. Commun. **6**, 8379 (2015).
[68] C. Rinaldi, M. Cantoni, D. Petti, A. Sottocorno, M. Leone, N. M. Caffrey, S. Sanvito, and R. Bertacco, Ge-based spin-photodiodes for room-temperature integrated detection of photon helicity, Adv. Mater. **24**, 3037 (2012).
[69] Y. Yang, R. C. da Costa, M. J. Fuchter, and A. J. Campbell, Circularly polarized light detection by a chiral organic semiconductor transistor, Nat. Photonics **7**, 634 (2013).
[70] M. Schulz, F. Balzer, D. Scheunemann, O. Arteaga, A. Lützen, S. C. J. Meskers, and M. Schiek, Chiral excitonic organic photodiodes for direct detection of circular polarized light, Adv. Funct. Mater. **29**, 1900684 (2019).
[71] J. Ahn, E. Lee, J. Tan, W. Yang, B. Kim, and J. Moon, A new class of chiral semiconductors: Chiral-organic-molecule-incorporating organic–inorganic hybrid perovskites, Mater. Horiz. **4**, 851 (2017).
[72] A. Ishii and T. Miyasaka, Direct detection of circular polarized light in helical 1D perovskite-based photodiode, Sci. Adv. **6**, 3274 (2020).
[73] Hamamatsu InGaAs quadrant photodiode (2021), accessed: 05/21/2021, https://www.hamamatsu.com/jp/en/product/type/G6849/index.html.
[74] Thorlabs InGaAs quadrant photodiode (2021), accessed: 05/21/2021, https://www.thorlabs.com/Images/PDF/Vol18_782-783.pdf.
[75] Ld-pd InGaAs quadrant photodiode (2021), accessed: 05/21/2021, http://www.ld-pd.com/?a=cpinfo&id=268.
[76] Hamamatsu income statement (2020), accessed: 05/24/2021, https://www.wsj.com/market-data/quotes/HPHTF/financials/annual/income-statement.
[77] R. K. Wangsness and F. Bloch, The dynamical theory of nuclear induction, Phys. Rev. **89**, 728 (1953).
[78] A. Redfield, The theory of relaxation processes, in *Advances in Magnetic Resonance*, edited by J. S. Waugh (Academic Press, IBM Watson Laboratory, Columbia University, New York, 1965), Vol. 1, p. 1–32.
[79] G. W. Leppelmeier and E. L. Hahn, Zero-field nuclear quadrupole spin-lattice relaxation in the rotating frame, Phys. Rev. **142**, 179 (1966).
[80] R. H. Masud Chaichian, *Symmetries in Quantum Mechanics: From Angular Momentum to Supersymmetry (Graduate Student Series in Physics)* (Taylor & Francis, Bristol and Philadelphia, 1997), 1st ed.